Hemilabile Thio– and Selenoethers in Bis(benzimidazolyl)Amine Copper Complexes Relevant to the Active Sites of Copper-Dependent Monooxygenases

Brenda Sánchez-Eguía, Hugo Hernández-Toledo, Sven Lidin, Marcos Flores-Alamo, Ebbe Nordlander, Sylvain Bertaina, Maylis Orio, Ivan Castillo

Hemilabile Thio– and Selenoethers in Bis(benzimidazolyl)amine Copper Complexes Relevant to the Active Sites of Copper-Dependent Monooxygenases

Brenda N. Sánchez-Eguía,[a] Hugo Hernández-Toledo,[b] Sven Lidin,[c] Marcos Flores-Alamo,[a] Ebbe Nordlander,[d] Sylvain Bertaina,[e] Maylis Orio,*[f] and Ivan Castillo*[b]

[a] Dr. Brenda N. Sánchez-Eguía, Dr. Marcos Flores-Alamo
Facultad de Química, División de Estudios de Posgrado, Universidad Nacional Autónoma de México, Circuito Exterior, CU, 04510, México
[b] M. Sc. Hugo Hernández-Toledo, Prof. Dr. Ivan Castillo
Instituto de Química, Universidad Nacional Autónoma de México, Circuito Exterior, CU, 04510, México
E-mail: *joseivan@unam.mx, ph: +5255 56224511, fax: +5255 56162217
[c] Prof. Dr. Sven Lidin
Center for Analysis and Synthesis, Lund University, Lund 221 00, Sweden
[d] Prof. Dr. Ebbe Nordlander
Chemical Physics, Department of Chemistry, Lund University, Box 124, Lund 221 00, Sweden
[e] Prof. Dr. Sylvain Bertaina
CNRS, Aix-Marseille Université, IM2NP (UMR 7334), Institut Matériaux Microélectronique et Nanosciences de Provence, Marseille, France
[f] Prof. Dr. Maylis Orio
Institut des Sciences Moléculaires de Marseille, Aix Marseille Université, UMR 7313, Avenue Escadrille Normandie-Niémen, 13397 Marseille Cedex 20, France
E-mail: *maylis.orio@univ-amu.fr, ph: +33413945613, fax: +330491289187

Supporting information for this article is given via a link at the end of the document.

Abstract: Copper complexes supported by benzimidazole-based tetradentate neutral ligands featuring thio- and selenoether donors, resemble the coordination environment of the active site in copper dependent monooxygenases Dopamine-β-monooxygenase (DβM) and peptidylglycine-α-hydroxylating monooxygenase (PHM). The cuprous complexes react with O_2 at low temperature generating a reactive copper-oxygen species assigned to a side-on cupric-superoxo complex, which activates the C-H bond of dihydroanthracene. Based on structural, ^{1}H and ^{77}Se NMR, and EPR spectroscopic characterization, together with DFT computations, the selenoether moiety likely acts as a hemilabile ligand in these scaffolds, which results in an electrophilic cupric-superoxide intermediate poised for H-atom transfer, as has been proposed for related bis(benzimidazole)-thioether analogues and selenoether-modified enzymatic systems.

Introduction

Dopamine-β-monooxygenase (DβM) and peptidylglycine-α-hydroxylating monooxygenase (PHM), two copper-dependent monooxygenase enzymes, have been the object of intense studies due to their capability to selectively activate aliphatic C-H bonds.[1–3] DβM catalyzes the hydroxylation of dopamine to norepinephrine, which is related to physiological and behavioral processes, as well as neurodegenerative diseases, e.g. Alzheimer.[4] The crystal structure of human DβM has been determined; the catalytic core has a similar conformation to that of PHM, with Cu_H and Cu_M domains 11 Å apart, and potential participation of a "closed" protein structure that places the copper binding domains at 4 Å.[5] PHM catalyzes the hydroxylation of terminal glycine peptides relevant to hormone synthesis; genetic evidence shows that the PHM domain is required for α-amidating activity of the PAM enzyme.[6–9]

In this context, several biomimetic approaches to gain understanding of the active catalytic species have been developed, which together with biochemical experiments have led to the proposal that the catalytic cycle starts with O_2 coordination to Cu_M.[10] Regardless of the active Cu-O_2 species responsible for the C-H activation,[11,12] copper-superoxo (Cu^{II}-$O_2^{\bullet-}$), copper-hydroperoxo (Cu^{2+}-OOH) and the putative copper-oxyl species (Cu^{II}-$O^{\bullet}$ ↔ Cu^{III}=O) have been associated with monooxygenase reactivity.[3,10-13] Evidence of a cupric-superoxo species was obtained in 2004 by Amzel *et al.* based on the report of the X-ray crystal structure of the precatalytic core of PHM, in which O_2 is bound in an end-on fashion Cu^{II}-η^1-$O_2^{\bullet-}$ (Figure 1).[14]

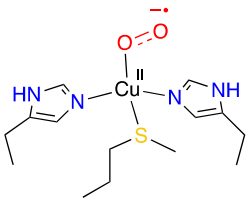

Figure 1. Schematic representation of the proposed Cu^{II}-η^1-$O_2^{\bullet-}$ active site of PHM.[14]

Model systems developed thus far include tri- and tetradentate ligands featuring N_xS_y (x,y = 0-4) as donor atoms,[15–23] with examples of Cu^{II}-$O_2^{\bullet-}$ complexes in both end-on and side-on binding modes.[24,25] The end-on Cu^{II}-η^1-$O_2^{\bullet-}$ complexes have a triplet ground state and an electrophilic character, acting as hydrogen atom transfer (HAT) agents toward weak C-H bonds;[26–28] the side-on Cu^{II}-η^2-$O_2^{\bullet-}$ complexes are generally characterized by a singlet ground state and tend to be unreactive toward organic substrates.[29,30] Our research group recently reported the first complexes formulated as side-on cupric-superoxo species based on the spectroscopic evidence available, with triplet ground states that enable them to activate the C-H bonds of dihydroanthracene (DHA) and THF.[31] This reactivity is related to the specific electronic properties of the benzimidazole-based ligands, and likely to the triplet ground state that they enforce.

Experimental and theoretical evidence indicate that the S atom of the thioether moiety in our model compounds acts as a hemilabile ligand.[31] To further scrutinize this behavior, as well as the role of the thioether donor in C-H activation, we have developed the new thio- and selenoether-based ligands bis(1-methyl-2-methylbenzimidazolyl)(phenylethyltioethyl)amine (**L^{SPh}**) and bis(1-methyl-2-methylbenzimidazolyl)(phenylselenoethyl)amine (**L^{Se}**, Scheme 1). The former ligand was devised to test the capability of our systems to activate the benzylic C–H bond of a potential internal substrate, following an intramolecular activation strategy that has been applied successfully in related ligand hydroxylations.[27,32] Thus, the benzylic position in **L^{SPh}** appears amenable to intermolecular hydroxylation, analogous to the case of dopamine in DβM.

In the latter ligand, ^{77}Se is an NMR active nucleus[33] that may be regarded as a sulfur analogue, considering that selenium is present in the so-called "21st essential aminoacid" selenocysteine.[34] Selenoether-containing ligands have been studied with diverse metal ions that showcase its wide range of applications.[35] To the best of our knowledge, these types of ligands have not been used in a biologically-inspired approach with Cu, with reports of Cu-selenoethers limited to structural studies.[36,37] Nonetheless, selenomethionine was recently used in protein-based biomimetic systems aimed at modeling PHM and its homologues,[38,39] including a proposed dicopper active site.[40] In our specific case, the presence of the Se atom in **L^{Se}** provides an additional spectroscopic handle through the NMR-active ^{77}Se; additionally, coupling of the S = ½ Se nucleus with Cu^{II} may be probed by EPR spectroscopy. Thus, we herein report the preparation of cuprous and cupric complexes of **L^{SPh}** and **L^{Se}** to investigate their electrochemical, spectroscopic, and structural properties, as well as their reactivities towards O_2 as relevant oxidative mimics of the active sites of copper monooxygenases (Scheme 1). Furthermore, **L^{Se}** was tested as a potential spectroscopic handle in these systems.

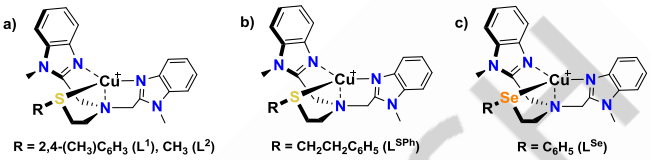

Scheme 1. a) Previously reported complexes; b) and c) analogous complexes studied in this work.

Results and Discussion

Ligand Characterization

Both ligands were obtained as off-white powders as described in the Electronic Supporting Information (ESI),[41,42] which were initially analyzed by IR spectroscopy as KBr pellets, with similar resonances characteristic of the benzimidazole groups: ν(C=N) resonances were observed at 1615 and 1612 cm^{-1} for **L^{SPh}** and **L^{Se}**, respectively. ^{1}H, ^{13}C and ^{77}Se NMR studies were performed to corroborate the identity of the samples. ^{1}H NMR spectroscopy revealed signals corresponding to the benzimidazole groups with similar δ values for both ligands. In the case of **L^{SPh}**, the signals at δ 3.57 (s, CH_3-NBzIm) and 3.94 (s, CH_2-N) ppm correspond to the N-methyl groups of the benzimidazole moieties and the methylene bridges between the central amine nitrogen and the benzimidazole carbon atom, respectively; the corresponding peaks for **L^{Se}** were observed at δ 3.70 (s, CH_3-NBzIm) and 4.05 (s, CH_2-N) ppm. ^{13}C NMR spectra showed 17 signals, 11 of them shifted to low field, assigned to the aromatic carbon atoms in the benzimidazole moieties in the case of **L^{SPh}**; 15 signals were observed for **L^{Se}**, consistent with its structure: four signals at high field, corresponding to the aliphatic carbon atoms, as well as 11 signals in the aromatic region. The ^{77}Se NMR spectra in Figure 2 show the signals of **L^{Se}** and its precursor: the amine **ASe** is characterized by a signal at 257 ppm; **L^{Se}** gives rise to a single peak at δ 279 ppm in $CDCl_3$. Further characterization of the ligands by DART MS confirmed their identity through the peaks observed at m/z = 470 and 490 for $[L^{SPh}]^+$ and $[L^{Se}]^+$, respectively (see Figures S7-S13).

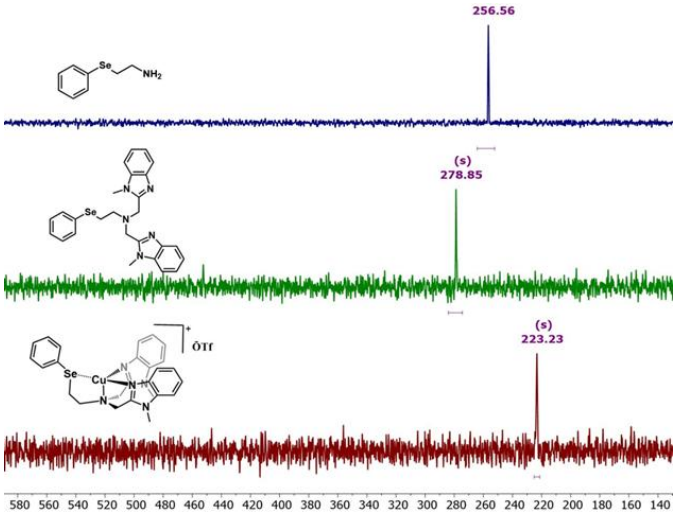

Figure 2. ^{77}Se NMR spectra: blue trace, **ASe**; green trace, **L^{Se}** in $CDCl_3$; red trace, [**L^{Se}**Cu]OTf in THF-d_8

Copper(I) complexes

Equimolar amounts of **L^{SPh}** or **L^{Se}**, and $[Cu(CH_3CN)_4]OTf$ were mixed in acetonitrile under an inert atmosphere. After evaporation of volatiles under reduced pressure, and washing of the obtained solids with diethyl ether, the complexes were isolated as pale-yellow solids in 47% ([**L^{SPh}**Cu]OTf) and 45% yield ([**L^{Se}**Cu]OTf). Vibrational analysis by IR spectroscopy was performed for both isolated solids, the resonances associated with the functional groups that participate in coordination of Cu exhibit were found to exhibit slight shifts toward lower frequencies.

^{1}H NMR spectroscopic characterization of [**L^{SPh}**Cu]OTf in THF-d_8 (Figure S14) reveals a broadening of the signals, as well as a slight displacement to low field relative to **L^{SPh}**. This is also the case for [**L^{Se}**Cu]OTf, which was further characterized by ESI MS in acetonitrile solution, revealing a peak at *m/z* = 552 consistent with monomeric [**L^{Se}**Cu]$^+$ formulation (Figures S15-S17); combustion analysis of the samples confirms their compositions. The broadness of the ^{1}H NMR spectrum of [**L^{Se}**Cu]OTf in THF-d_8 was interrogated in the temperature range of 10 to -60ºC, with the signal corresponding to the NCH_2-benzimidazole linker giving rise to two separate peaks starting at 10ºC (Figure S18). Acquisition of ^{77}Se NMR data from 10 to -60ºC resulted in silent spectra that did not allow addressing a potential dynamic process involving the selenoether donor; broadening of ^{77}Se NMR signals has been previously reported in selenomethionine-containing proteins.[43] While the variable temperature NMR analysis is inconclusive, room temperature ^{77}Se NMR spectra of [**L^{Se}**Cu]OTf in THF-d_8 show a single peak at 223 ppm (Figure 1), indicating a bound selenoether donor in the cuprous complex in solution.[44]

To further probe the solution behavior of both [**L^{SPh}**Cu]$^+$ and [**L^{Se}**Cu]$^+$, 2D DOSY NMR studies were performed; this technique has been extensively employed to prove the monomeric nature of related Cu^I complexes.[21] Thus, 3 mM THF-d_8 solutions were analyzed by this technique, and the results confirm the monomeric nature of both complexes (Table 1, and Figures S19 and S20). The diffusion coefficients (*D*) obtained from the experiments for the free ligands were used as reference for calculation of the hydrodynamic radii (rH) from the Stokes-Einstein equation.[45] Assuming spherical molecules, *D* for a compound analyzed by this technique may be correlated with its approximate size according to the calculated rH. The *D* values (Table 1) obtained for [**L^{SPh}**Cu]OTf and [**L^{Se}**Cu]OTf are only ~2.5 Å and 1.5 Å larger than those determined for **L^{SPh}** and **L^{Se}**; this led us to conclude that both cuprous complexes are mononuclear in solution, since a much larger difference in rH would have been measured for dimeric complexes relative to the parent ligands. Moreover, coordination of acetonitrile can be neglected, since its residual solvent peak at 2.0 ppm shows considerably larger diffusivity, consistent with free CH_3CN (Figures S19 and S20).

Table 1. Diffusion coefficients (*D*) and hydrodynamic radii (rH) determined for **L^{SPh}**, **L^{Se}**, and their cuprous complexes.

Compound	*D* (x 10^{-10} m^2/s)	rH (Å)
L^{SPh}	8.696	5.45
[**L^{SPh}**Cu]OTf	6.647	7.13
L^{Se}	9.387	5.05
[**L^{Se}**Cu]OTf	7.204	6.58

Copper(II) complexes

Cupric complexes were obtained by mixing equimolar amounts of the ligands and $Cu(H_2O)_6(OTf)_2$ (OTf^- = $CF_3SO_3^-$) in acetonitrile at room temperature, followed by trituration with diethylether; $Cu(H_2O)_6OMes_2$ ($OMes^-$ = $CH_3SO_3^-$) was employed to obtain single crystals of a cupric **L^{Se}** derivative exclusively. The green solid retrieved in the case of **L^{SPh}** was formulated as [**L^{SPh}**CuCl]OTf, and isolated in 92% yield; mixed anion complexes have been obtained previously from **L^{SPh}**·HCl, since bis(benzimidazolyl)amines tend to act as proton sponges.[22,23,31] [**L^{Se}**Cu(H_2O)](OTf)$_2$ and [**L^{Se}**Cu(H_2O)]$OMes_2$ were isolated in 98% and 88% yields. Initial characterization by ESI MS, evidenced their mononuclear nature in acetonitrile solution. The peaks at *m/z* = 567.3 and 681.2 were assigned to [**L^{SPh}**CuCl]$^+$ and [**L^{SPh}**Cu(OTf)]$^+$, respectively (Figure S22). Likewise, the peak at *m/z* = 701.0 was assigned to [**L^{Se}**Cu(OTf)]$^+$ (Figure S25), and the one at *m/z* = 647.0 to [**L^{Se}**Cu(OMes)]$^+$. Combustion analysis is consistent with the proposed formulae. Further characterization in CH_3CN solution by optical spectroscopy revealed in all cases strong absorption bands below 300 nm, assigned as intraligand transitions. For [**L^{SPh}**CuCl]OTf, a S→Cu LMCT band was observed at λ = 343 nm (ε = 2201 $M^{-1}cm^{-1}$),

while the *d-d* band was detected at λ = 634 nm (ε = 81 $M^{-1}cm^{-1}$). In the case of [L^{Se}Cu(H_2O)]($OTf)_2$, the shoulder at λ = 344 nm (ε = 1167 $M^{-1}cm^{-1}$) was assigned as a Se→Cu LMCT band, in analogy with related absorption bands observed for Cu-thioether complexes;[22,23] additionally, the *d-d* transition at λ = 689 nm (ε = 101 $M^{-1}cm^{-1}$) is consistent with a square pyramidal coordination geometry (see Figures S21-S26).[46]

EPR spectra of the two complexes were recorded at 77 K from frozen solutions using CH_3CN (Figures S27 and S28) or CH_3OH and the results confirmed the axial geometry around the Cu^{II} centers. Figure 3 presents the best-resolved experimental EPR spectra of [L^{Se}Cu(H_2O)]($OTf)_2$ obtained in CH_3OH together with its simulation with the Easyspin program package. The best fit provides values of $g_{\parallel}$ = 2.278 with $A_{\parallel}$ = 494 MHz (164 × 10^{-4} cm^{-1}) and $g_{\perp}$ = 2.061 with $A_{\perp}$ = 16 MHz (5 × 10^{-4} cm^{-1}), Figure 3. For [L^{SPh}CuCl]OTf recorded in CH_3CN (Figure S28), we obtained features at $g_{\parallel}$ = 2.254 with $A_{\parallel}$ = 542 MHz (180 × 10^{-4} cm^{-1}) and $g_{\perp}$ = 2.056 with $A_{\perp}$ = 27 MHz (9 × 10^{-4} cm^{-1}). There is a significant difference in the $g_{\parallel}$ and $A_{\parallel}$ parameters for the two complexes: calculation of the distortion factor *f*,[47] with $f = g_{\parallel}/A_{\parallel}$, affords values of 139 and 125 for [L^{Se}Cu(H_2O)]($OTf)_2$ and [L^{SPh}CuCl]OTf, respectively, indicating a higher degree of distortion from an ideal square pyramidal geometry for the former complex. This is also confirmed in the solid-state structures (*vide infra*), where the larger Se atom appears to pull the Cu^{II} ion out of the equatorial plane defined by the benzimidazole and amine N-donors.

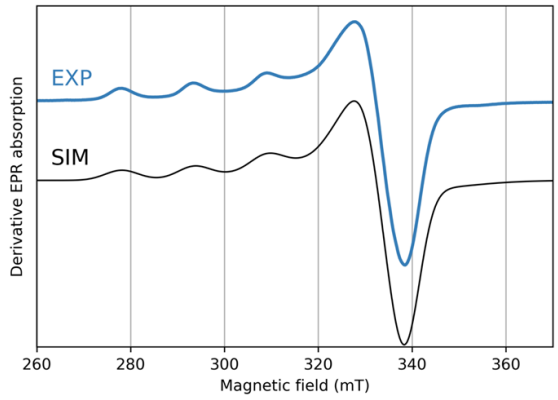

Figure 3. Experimental and simulated EPR spectra of [L^{Se}Cu(H_2O)]($OTf)_2$ in CH_3OH recorded at 77 K. Conditions: frequency 9.6279 GHz, microwave power 20 mW and field modulation 0.5 mT.

Solid-state structures

X-ray quality crystals of [L^{SPh}Cu]OTf were obtained by slow evaporation of a concentrated acetonitrile solution. The solid-state structure consists of dimeric [L^{SPh}Cu]$_2^{2+}$, with the three nitrogen atoms from the benzimidazole and central amine as donors, and the thioether moieties completing the coordination environment as bridging ligands towards Cu^{I} ions in the crystallographically related monomeric unit opposite to it (Figure 4). This behavior has been observed in related systems,[22,31] as well as the distorted tetrahedral geometry around the Cu^{I} centers (τ_4 = 0.73, with τ_4 = 0 for a square planar and τ_4 = 1 for a tetrahedral geometry).[48] Crystallographic data are presented in Table S1.

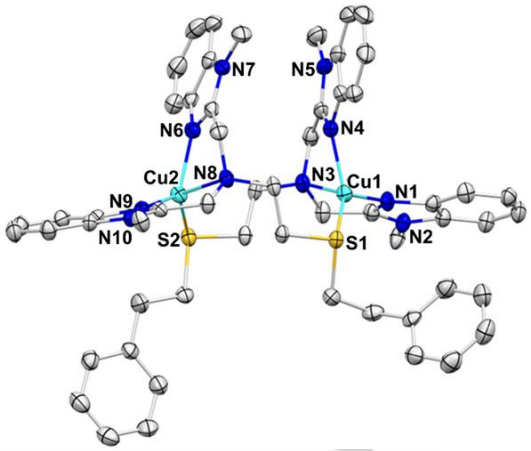

Figure 4. Solid state structure of [L^{SPh}Cu]$_2$($OTf)_2$ with thermal ellipsoids at the 50% probability level, H atoms and triflate anions omitted for clarity. Color code: Cu, turquoise; N, blue; S, yellow; C, gray.

X-ray quality crystals of [L^{SPh}CuCl]OTf, [L^{SPh}Cu(NO_3)]OTf, and [L^{Se}Cu(H_2O)]$OMes_2$ were obtained by slow evaporation of concentrated methanolic solutions. The first one has a square-pyramidal geometry around the Cu^{II} center (τ_5 = 0.25; τ_5 = 0 for a square pyramid and τ_5 = 1 for a trigonal bipyramid).[49] [L^{SPh}CuCl]OTf features a thioether moiety in the axial position, placing it as a weak donor [Cu–S bond distance 2.6512(14) Å]; the three nitrogen atoms are in equatorial positions, and the fourth equatorial position is occupied by the chloride ligand (Figure 5a). It is noteworthy that the distance between the Cl atom and the hydrogen atoms in the benzylic position is ~3.785 Å, which would be relevant to the reactivity of the cuprous [L^{SPh}Cu]OTf towards dioxygen if the thioether moiety remains bound in the reactive copper-oxygen species. In attempts to remove the residual chloride that is presumably retained from ligand synthesis as L^{SPh}·HCl, ethanolic solutions of L^{SPh} were treated with an equimolar amount of $AgNO_3$, which resulted in the formation of crystals of [L^{SPh}Cu(NO_3)]OTf. The metal center has a pseudo-octahedral geometry, with the nitrate ion acting as a bidentate ligand (Figure 5b). The sum of the angles for an ideal octahedron is 1620° in this case the sum is 1512°, resulting in a calculated 7% distortion.[50] A summary of interatomic distances and selected angles is presented in Table S2.

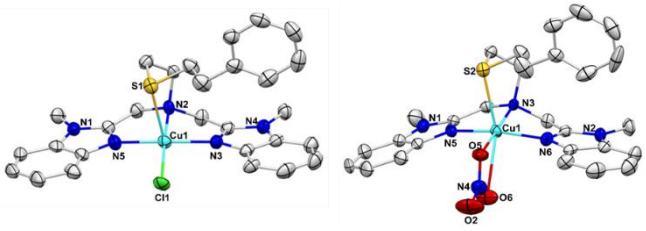

a) b)

Figure 5. Solid state structures of: a) [L^{SPh}CuCl]OTf, and b) [L^{SPh}Cu(NO_3)]OTf with thermal ellipsoids at the 50% probability level; H atoms and triflate anions omitted for clarity. Color code: O, red; Cl, green. S atoms are stereogenic centers, the enantiomers are contained within the centrosymmetric unit cells.

The solid-state structure of [L^{Se}Cu(H_2O)]$OMes_2$ is characterized by three nitrogen atoms of the benzimidazole moiety and the central amine defining the equatorial plane (Figure 6); the $OMes^-$ anions do not coordinate to the metal center, and instead a molecule of water occupies the fourth position of the pyramidal base. The selenoether donor is placed in the axial position, in an analogous fashion to the thioether donors in related complexes [Cu–Se bond distance 2.7371(4) Å]. The slightly larger degree of distortion (τ_5 = 0.27) can be attributed to the size of the Se atom, as is also reflected in the parameters determined by EPR spectroscopy. Although the presence of the selenium bound to the cupric ion in [L^{Se}Cu(H_2O)]$OMes_2$ contrasts with the evidence against such interaction obtained by EXAFS in the Se-containing PHM protein model reported by Blackburn and coworkers,[39] the latter data may indicate that Se (and S in PHM) are present in a weakly interacting axial position.[51]

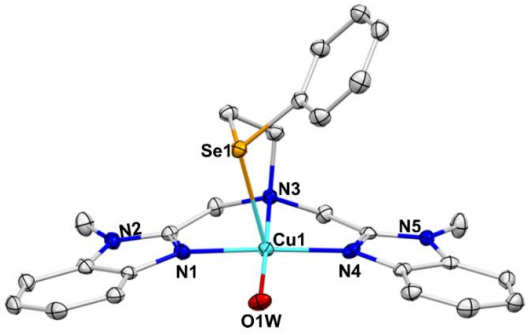

Figure 6. Solid state structure of [L^{Se}Cu(H_2O)]$OMes_2$ with thermal ellipsoids at the 50% probability level, H atoms and mesylate counterions omitted for clarity. Color code: Se, orange.

Electrochemical studies

Cyclic voltammetry studies were carried out to obtain the redox potential for the $Cu^{II/I}$ couples in the coordination environment provided by the ligands. L^{SPh} is characterized by oxidation peaks at E_{ap}^{I} = 0.75, E_{ap}^{II} = 1.20, and E_{ap}^{III} = 1.33 V in acetonitrile solution (Figure S29), while L^{Se} presents four oxidation peaks at E_{ap}^{I} = 0.74, E_{ap}^{II} = 0.96, E_{ap}^{III} = 1.22, and E_{ap}^{IV} = 1.67 V [relative to the ferricenium/ferrocene couple (Fc^+/Fc)]. These ligand-centered redox processes shift anodically upon coordination of the metal ion, while the copper-centered process $Cu^{II/I}$ for [L^{Se}Cu]OTf was measured at $E_{1/2}$ = -0.15 V vs Fc^+/Fc, with a quasi-reversible behavior (ΔE = 140 mV, Figure 7). In contrast, the redox potential for [L^{SPh}Cu]OTf was measured at $E_{1/2}$ = -0.17 V vs Fc^+/Fc, and ΔE = 340 mV corresponding to an irreversible behavior (Figures S29-S31). With respect to related thioether systems,[22,23] the less negative redox potential for the [L^{Se}Cu]$^{2+/+}$ couple is in line with the expected preference of the soft Cu^I ion for the selenoether donor. Nonetheless, the difference is small enough so that the L^{Se} can be considered a reasonable analogue of the thioether-based ligands previously employed. A summary of $E^{1/2}$ values for the systems studied in this work is presented in Table 2.

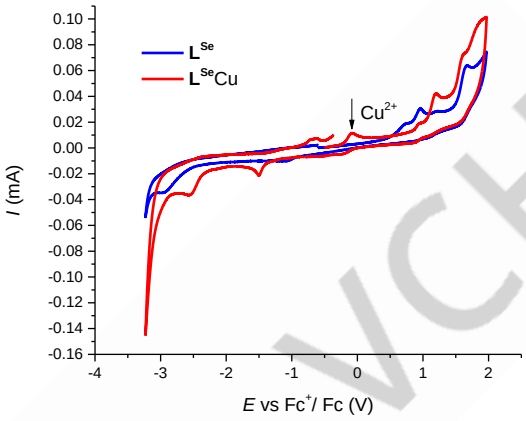

Figure 7. Cyclic voltammograms of L^{Se} (blue trace) and [L^{Se}Cu]OTf (red trace).

Table 2. Half-wave potentials of the $Cu^{II/I}$ couples (vs Fc^+/Fc).

Complexes	[L^{SPh}Cu]$^{2+/+}$	[L^{Se}Cu]$^{2+/+}$
$E_{1/2}$ (mV)	-170	-150
ΔE (mV)	340	140

Reactivity studies

Reaction of the cuprous complexes with O_2 was performed at -80°C in THF solution, resulting in immediate spectral changes in the UV-vis spectra, which remain constant for at least 2 h; both [L^{SPh}Cu]OTf and [L^{Se}Cu]OTf presented similar behavior after bubbling of O_2 for one minute through the solutions, with bands at λ = 336 (ε = 1905 and 1772 M^{-1} cm^{-1} respectively). These have been associated with the charge transfer from a superoxo ligand bound to Cu^{II} in a side-on fashion, Cu^{II}-η^2-$O_2^{\bullet-}$.[24] Formation of peroxo dicopper complexes was excluded based the lack of changes in the optical spectra upon addition of up to 3 equivs. of $CH_3SO_3^-$ or benzoate to the THF solutions of the putative Cu^{II}-η^2-$O_2^{\bullet-}$ complexes at -80°C that typically result in the stabilization of the former Cu^{II}_2-μ-η^2:η^2-O_2^{2-} peroxo dicopper species.[52,53] Moreover, the putative peroxo dicopper and related cupric hydroperoxo Cu^{II}-OOH complexes were independently generated by addition of 10 equivs. of H_2O_2/NEt_3 mixture to THF solutions of [L^{SPh}/L^{Se}Cu(S)]$(OTf)_2$ at -60°C (S = solvent). The optical features are consistent with a mixture of Cu^{II}_2-μ-η^2:η^2-O_2^{2-} (λ = 352-356 nm) and Cu^{II}-OOH (λ = 309-311 nm, Figure 8a), which have been shown to interconvert in solution with supporting tridentate ligands, but not with tetradentate ones.[54] The latter point further supports the hemilability of the chalcogen

ethers that render $\mathbf{L^{SPh}}$ and $\mathbf{L^{Se}}$ tridentate upon decoordination of S or Se. Thus, distinct UV-vis spectra arising from cupric side-on superoxo, dicopper side-on peroxo, and cupric-hydroperoxo can be identified at low temperature (Figure 8b), as further supported by DFT calculations (*vide infra*). Unfortunately, these systems fluoresce strongly when excited at 340 nm, thus precluding resonance Raman studies for further confirmation of their proposed structures.

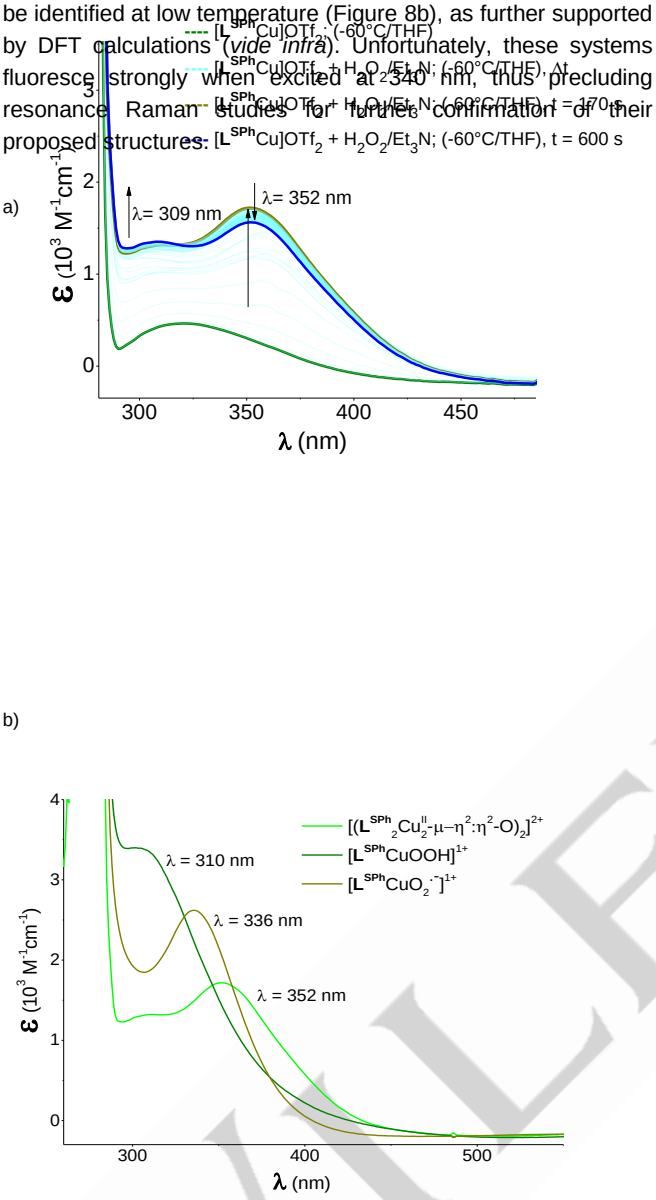

Figure 8. a) UV-vis spectra of 0.3 mM [$\mathbf{L^{SPh}}$Cu(S)](OTf)$_2$ at -60°C in THF upon addition of 10 equivs. H_2O_2/NEt_3, resulting in a mixture of of Cu^{II}_2-μ–η^2:η^2-O_2^{2-} (λ = 352 nm) and Cu^{II}-OOH (λ = 309-310 nm) species; b) comparative UV-vis spectra of the independently generated copper-oxygen species.

The capability of the cupric superoxo complexes to perform C-H bond activation was evaluated using 9,10-dihydroanthracene (DHA) as substrate with the preformed Cu^{II}-η^2-$O_2^{\bullet-}$ at -60°C under pseudo-first order conditions, Figures 9 and S32-S34. The putative cupric-superoxo complexes were generated at -80°C, but the reactions were carried out with DHA at -60°C to achieve appreciable rates. Thus, decrease of the intensity of the charge transfer band was monitored by UV-vis spectroscopy, as this has been associated with reaction of the cupric-superoxo complex with DHA through hydrogen atom abstraction (HAT), with pseudo-first order kinetic constants of k = 3.02 ± 0.11 × 10^{-4} s^{-1} ($t_{1/2}$ = 2294 s) and k = 1.2 ± 0.12 × 10^{-3} s^{-1} ($t_{1/2}$ = 578 s) starting from [$\mathbf{L^{SPh}}$Cu]OTf and [$\mathbf{L^{Se}}$Cu]OTf, respectively; the corresponding reactions with deuterated DHA-d_4 were too slow under the same conditions to allow the determination of a kinetic isotope effect. Gas chromatography-mass spectrometry (GC-MS) experiments confirmed the identity of the oxidation products, showing the characteristic retention times and observed *m/z* values of anthracene (12.57 min, 12%), anthrone (13.62 min, 20%), and anthraquinone (13.75 min, 34% chromatographic yields) for the reaction with [$\mathbf{L^{SPh}}$Cu]OTf; overoxidation products have been previously detected in these types of transformations.[55] In the reaction of [$\mathbf{L^{SPh}}$Cu]OTf with 100 equivs. DHA, consumption of the generated cupric superoxo proceeds cleanly as evidenced by an isosbestic point, which is accompanied by the formation of the corresponding cupric hydroperoxo upon HAT (λ_{max} = 310 nm, Figure 9).

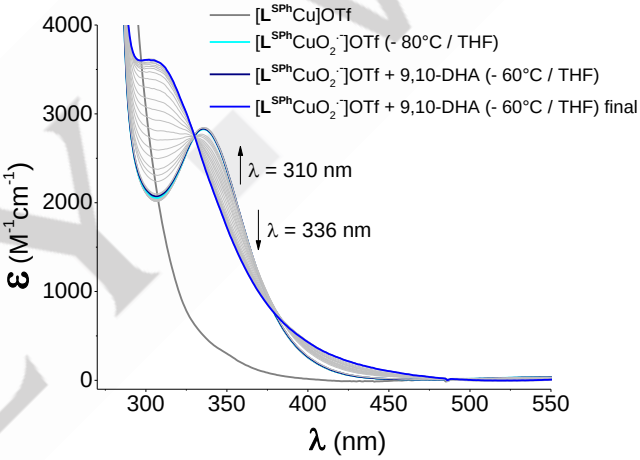

Figure 9. UV-vis spectra of $\mathbf{L^{SPh}}Cu^{II}$-η^2-$O_2^{\bullet-}$ generated at -80°C in THF, after bubbling O_2 for one min ((λ_{max} = 336 nm, light blue trace), and addition of 100 equivs. 9,10-DHA at -60°C; the final spectrum is assigned to the Cu^{II}-OOH complex formed after HAT (λ_{max} = 310 nm, dark blue trace).

For [$\mathbf{L^{Se}}$Cu]OTf, the reaction proceeds smoothly with 10 equivs. DHA, with evidence of formation of the cupric hydroperoxo (λ_{max} = 312 nm, Figure S36) as in the case of [$\mathbf{L^{SPh}}$Cu]OTf. However, the use of 35-100 equivs. DHA resulted in virtually no further changes. This observation can be attributed to inhibition by small amounts of DHA oxidation products, evidencing different reactivity for the selenoether analog that must be taken into consideration when replacing S with Se in these types of studies. Further analysis of the in situ generated cupric-superoxo complexes by EPR spectroscopy showed essentially silent reaction mixtures. The samples were compared to $Cu(OTf)_2$ as external standard: before the reaction, integration for [$\mathbf{L^{SPh}}$Cu]OTf and [$\mathbf{L^{Se}}$Cu]OTf in THF solution corresponded to 3.5 and 6.8% oxidized species, respectively; this is attributed to adventitious air oxidation (Figures S37-S39). After bubbling O_2 through the solutions, the percentages measured were 7.5 and 16%, respectively, indicating that most of the copper-oxygen

species present are EPR-silent. The parameters observed for the minor EPR-active cupric species generated upon O_2 bubbling through solutions of [$\mathbf{L}^{SPh}$Cu]OTf and [$\mathbf{L}^{Se}$Cu]OTf are *g* = 2.055; 2.076; 2.261 with A = 10; 10; 523 MHz, and *g* = 2.032; 2.088; 2.256 with A = 10; 50; 501 MHz, respectively (Figures S40 and S41). We assign these to small amounts of cupric-hydroperoxo complex formation due to rapid HAT reaction of the cupric superoxo complexes with solvent (THF). Unfortunately, no reaction that could be attributed to intramolecular hydroxylation was detected under the experimental conditions, so that C-H activation at the benzylic position of the -SCH_2CH_2Ph fragment of [$\mathbf{L}^{SPh}$Cu]$^+$ is not favored. This observation supports the hemilability of the thioether moiety in the proposed [$\mathbf{L}^{SPh}Cu^{II}$-η^2-$O_2^{\bullet-}$]$^+$, since hydroxylation would be expected if a Cu-S bond kept the -SCH_2CH_2Ph group in the proximity of the electrophilic Cu^{II}-η^2-$O_2^{\bullet-}$ O-atoms.

Computational studies

Density functional theory calculations (DFT) were performed to understand the electronic structures of the starting copper complexes, to elucidate the nature the reactive copper-oxygen species generated, and to gain insight into the observed reactivity. The starting complexes were first subjected to geometry optimizations for comparison with the solid-state structures for benchmarking (Figures S42-S47). Electronic structure calculations provided singly occupied molecular orbitals (SOMOs) for both [$\mathbf{L}^{SPh}$CuCl]$^+$ and of [$\mathbf{L}^{Se}$Cu(H_2O)]$^{2+}$ that are metal-based orbitals with predominant Cu 3*d*x^2-y^2 character (Figure 10) while the spin density was found mainly distributed on the copper center and its coordinating atoms using Mulliken population analysis (Table S3). The two complexes are Cu^{II} species with doublet ground spin states, *S* = 1/2.

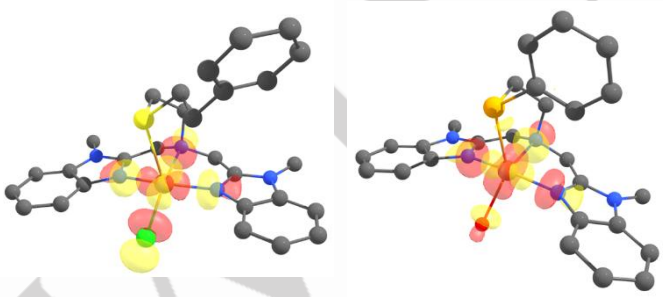

Figure 10. Localized SOMOs of [$\mathbf{L}^{SPh}$CuCl]$^+$ (left) and [$\mathbf{L}^{Se}$Cu(H_2O)]$^{2+}$ (right). Hydrogen atoms omitted for clarity, color code: S, yellow and Se, light orange.

Experimental and simulated EPR parameters of the two complexes were further studied by computations performed on various DFT models, varying the nature of the exogenous ligand bound to the copper center to account for the experimental conditions (Tables S4 and S5). To assess the agreement between theory and experiment (Table 4), we examined the axial and rhombic shift parameters (g_{max}, A_{max}^{Cu}, Δg_{max} and $\Delta A_{max\text{-}min}^{Cu}$) as well as the isotropic values (g_{iso}, A_{iso}^{Cu}). The results presented in Tables 4 and S4 show that the DFT model having a chloride bound to the copper center reproduces quantitatively well the main features of the EPR spectrum of [$\mathbf{L}^{SPh}$CuCl]OTf in CH_3CN. The calculated data suggest that the solid-state structure of the complex is maintained in frozen solution. From Tables 4 and S5, a good agreement is found between experiment and theory when considering the DFT model having a methanol molecule bound to the copper centre and the EPR spectrum of [$\mathbf{L}^{Se}$Cu(H_2O)]$(OTf)_2$ in MeOH. These data point at the exchange of the coordinated water molecule found in the solid-state structure by a methanol once in methanolic solution, followed by deprotonation. The SOMO obtained from electronic structure calculations on [$\mathbf{L}^{Se}$Cu(OCH_3)]$^+$ is also a metal-based orbital (Figure 11) with significant spin density found at the copper center and its coordinating atoms (Table S6).

Table 4. Comparison between computed *g*-values and copper hyperfine coupling constants of the relevant DFT-models with experimental EPR data.

	g_{min}	g_{mid}	g_{max}	g_{iso}	Δg_{min}	Δg_{mid}	Δg_{max}	Δg_{iso}
[$\mathbf{L}^{SPh}$CuCl]$^+$	2.050	2.097	2.249	2.132	0.048	0.095	0.247	0.130
Expt.	2.056	2.056	2.254	2.121	0.054	0.054	0.252	0.119
[$\mathbf{L}^{Se}$Cu(OCH_3)]$^+$	2.050	2.092	2.267	2.137	0.048	0.090	0.265	0.135
Expt.	2.061	2.061	2.278	2.133	0.059	0.059	0.276	0.131
	A_{min}	A_{mid}	A_{max}	A_{iso}	$\Delta A_{mid\text{-}min}$	$\Delta A_{max\text{-}mid}$	$\Delta A_{max\text{-}min}$	
[$\mathbf{L}^{SPh}$CuCl]$^+$	18	75	540	211	57	465	522	
Expt.	27	27	542	199	0	515	515	
[$\mathbf{L}^{Se}$Cu(OCH_3)]$^+$	77	100	496	224	23	396	419	
Expt.	16	16	494	175	0	478	478	

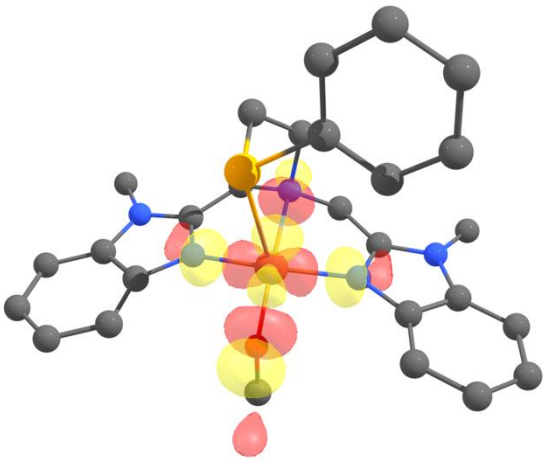

Figure 11. Localized SOMO of $[L^{Se}Cu(OCH_3)]^+$. Hydrogen atoms omitted for clarity, color code: Se, light orange.

For a better understanding of the optical properties of the two starting complexes, TD-DFT calculations were undertaken on DFT-models having either Cl, H_2O or CH_3CN as exogenous ligands to assign the salient features of the experimental UV-vis spectra by computing the main transition energies and their relative intensities. Considering $[L^{SPh}Cu(CH_3CN)]^{2+}$ and $[L^{Se}Cu(CH_3CN)]^{2+}$ as models, their optical properties are adequately reproduced (Figures S44-S47, and Table S7).

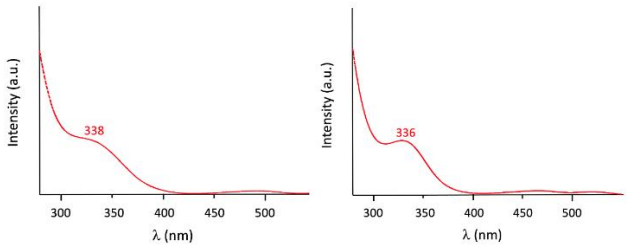

Figure 12. Theoretical fit of the UV-vis spectra of $[L^{SPh\text{-}decoord}CuO_2]^+$ (left) and $[L^{Se\text{-}decoord}CuO_2]^+$ (right).

Once the calculated properties of the starting complexes were compared to the experimental ones, DFT calculations were then performed to elucidate the structure of the reactive copper-oxygen species generated and corroborate the experimentally observed UV-vis. Following previous work from our group,[31] a set of structural models was constructed considering monomeric end-on cupric-superoxo complexes in the triplet state, S = 1, with either coordinated or decoordinated thioether and selenoether groups (Figures S48-S50). To evaluate the relevance of these models, their optical properties were computed by TD-DFT calculations for comparison with the experimental UV-vis spectra (Figures 8, 9 and S36). A good agreement with respect to the experimental data is obtained with the $[L^{SPh\text{-}decoord}CuO_2]^+$ and $[L^{Se\text{-}decoord}CuO_2]^+$ complexes having decoordinated thioether and selenoether groups (Figures 12 and S50). Our calculations adequately reproduce the key feature of the spectra, namely the bands at 336 nm and provide electronic transitions at λ_{max} = 338 and 336 nm (f = 0.023 and 0.020) for $[L^{SPh\text{-}decoord}CuO_2]^+$ and $[L^{Se\text{-}decoord}CuO_2]^+$, respectively (Figure 12 and Table S11). The difference density plots presented in Figure S51 show that the electronic transitions contributing to the intense absorption found at 336-338 nm are due to excitations from the copper center to the superoxo moiety.

For $[L^{SPh\text{-}decoord}CuO_2]^+$, electronic structure calculations show that the two unpaired electrons of the complex are strongly ferromagnetically coupled, consistent with a triplet ground spin state that is stabilized by 8.5 kcal mol^{-1} relative to the corresponding singlet. Similar results were obtained for $[L^{Se\text{-}decoord}CuO_2]^+$ with the triplet also being the favored ground spin state by 8.6 kcal mol^{-1} (Figure 13). High spin states were expected for both cases due to the orthogonality of the two magnetic orbitals of $[L^{SPh\text{-}decoord}CuO_2]^+$ and $[L^{Se\text{-}decoord}CuO_2]^+$, which are depicted in Figures 13 and S52. The first one is a superoxo-centered π_v* orbital perpendicular to the Cu–OO plane, while the second one corresponds to the antibonding interaction

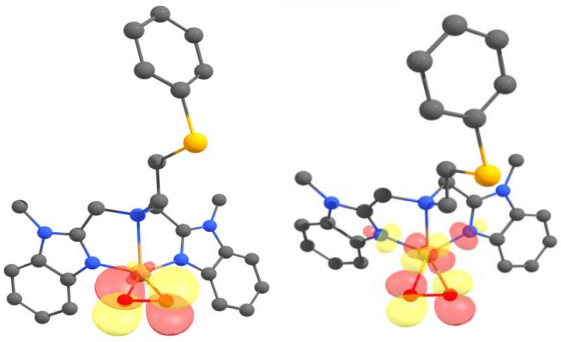

between the Cu dx^2-y^2 and the π_σ* orbitals. Mulliken spin population analysis of the two models provides a similar picture with significant spin density found at the copper center and the superoxyl ligands (Table S12).

Figure 13. Localized SOMOs of $[L^{Se\text{-}decoord}CuO_2]^+$.

To gain insight into the nature of the minor EPR-active cupric species generated upon O_2 bubbling and subsequent H-abstraction (from THF solvent), DFT calculations were performed on putative models including a hydroperoxo ligand in equatorial position and considering either coordination or decoordination of the thioether and selenoether moieties from the copper centers (Figures S53 and S54). To discriminate between these scenarios, the EPR parameters of the models were confronted with experimental data (Tables S13 and S14). The agreement between theory and experiment was assessed based on the axial and rhombic shift parameters as well as the isotropic values. Comparison between computed and simulated EPR parameters show that the DFT models having a OOH^- ligand bound to the copper center with decoordinated thioether and selenoether moieties reproduce quantitatively well the main features of the experimentally-observed EPR spectra. The

SOMOs obtained from electronic structure calculations on [$\mathbf{L}^{\mathbf{SPh\text{-}decoord}}$Cu(OOH)]$^+$ and [$\mathbf{L}^{\mathbf{Se\text{-}decoord}}$Cu(OOH)]$^+$ are Cu dx^2-y^2 orbitals (Figure 14) with spin density being spread over the copper centers, the coordinated nitrogen atoms and the hydroperoxo ligand (Table S15). EPR data are thus consistent with doublet ground spin state S = 1/2 Cu^{II}-OOH species.

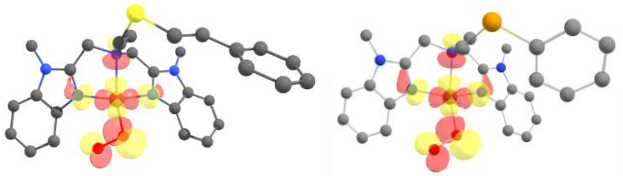

Figure 14. Localized SOMOs of [$\mathbf{L}^{\mathbf{SPh\text{-}decoord}}$CuOOH]$^+$ (left) and [$\mathbf{L}^{\mathbf{Se\text{-}decoord}}$CuOOH]$^+$ (right).

The experimental assignment of the cupric hydroperoxo species is further supported by the predicted optical properties computed by TD-DFT calculations and compared with the experimental UV-vis spectra (Figures 8, 9 and S36). Our calculations on [$\mathbf{L}^{\mathbf{SPh\text{-}decoord}}$Cu(OOH)]$^+$ and [$\mathbf{L}^{\mathbf{Se\text{-}decoord}}$Cu(OOH)]$^+$ reasonably reproduce the main feature of the experimental UV-vis spectra, namely the bands at 310 and 312 nm and provide electronic transitions at λ_{max} = 278 and 277 nm (f = 0.012 and 0.019), respectively (Figures 15 and S55 and Table S16). The electronic transitions contributing to the main absorption found at 278 and 277 nm, blueshifted relative to those observed for the corresponding cupric-superoxos, are assigned to ligand-to-metal charge transfers (LMCT) based on the difference density plots presented in Figure S56.

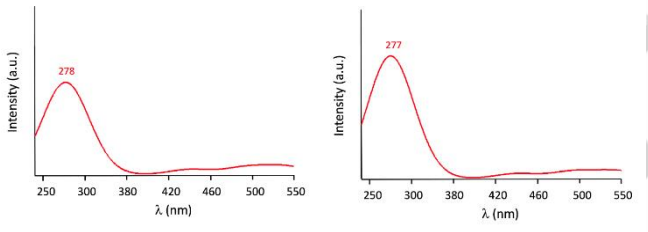

Figure 15. Theoretical fit of the UV-vis spectra of [$L^{SPh\text{-}decoord}$CuOOH]$^+$ (left) and [$L^{Se\text{-}decoord}$CuOOH]$^+$ (right).

Our calculations suggest that the generated cupric-hydroperoxo species retain the characteristics of the cupric-superoxo generated upon intial interacion of Cu^I complexes with O_2, for which DFT calculations showed that the thioether and selenoether moieties remain decoordinated from the metal centers.

Mechanistic proposal

The combined observations demonstrate the capability of the $\mathbf{L}^{\mathbf{SPh}}$/$\mathbf{L}^{\mathbf{Se}}$ copper complexes to act as bioinspired platforms for the activation of O_2, and subsequent HAT from 9,10-DHA as a model substrate. The cuprous complexes react with O_2, generating the putative *side-on* cupric superoxo complexes that activate intermolecularly the C-H bonds of 9,10-DHA, resulting in transient formation of the corresponding Cu^{II}-OOH complex. The inertness of the potentially reactive intramolecular benzylic position in $\mathbf{L}^{\mathbf{SPh}}Cu^{II}$-$\eta^2$-$O_2^{\bullet-}$ suggests that it may not be adequately positioned for C-H activation, supporting the notion that the chalcogen ether acts as a hemilabile ligand, both in model systems and in DβM and PHM, as proposed for selenomethionine mutants.[39] However, replacement of S by Se must be carefully considered, since the H-abstraction capability may be modified, as is the case in the $\mathbf{L}^{\mathbf{Se}}$-based system described. Nevertheless, initial HAT appears to result in both cases in the corresponding cupric hydroperoxos, which may transfer the hydroxy group to the organic radical generated, as shown in Scheme 2. Subsequent activation of the more reactive hydroxylated 9-OH-10-hydroanthracene results in the observed anthrone and anthraquinone as overoxidation products. Although this mechanism does not consider the potential involvement of dicopper sites in HAT as has been proposed for the closed conformations of DβM and PHM,[56] the evidence presented for such species so far is mainly theoretical,[57] and the closed enzymatic conformation has only been observed when copper is vacant in one of the sites.[58]

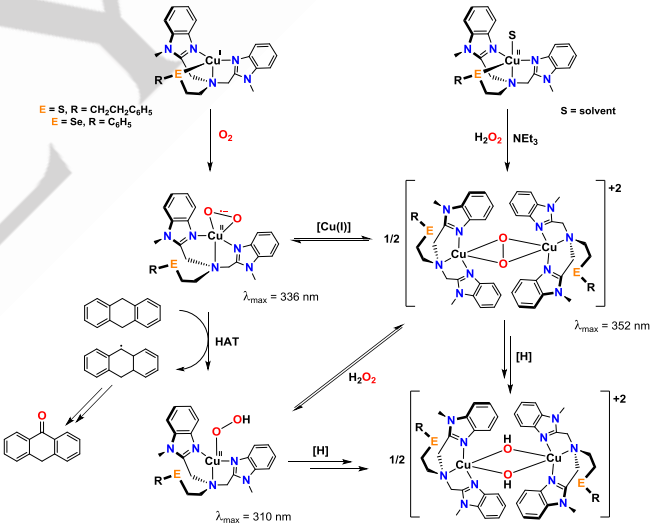

Scheme 2. Copper-oxygen species relationship and mechanistic proposal for HAT by [$\mathbf{L}^{\mathbf{SPh}}$/$\mathbf{L}^{\mathbf{Se}}Cu^{II}$-$\eta^2$-$O_2^{\bullet-}$]OTf.

Conclusion

Bis(benzimidazole)amino thio/selenoether ligands stabilize both cuprous and cupric complexes. This ligand platform allows the Cu^I complexes to selective activate dioxygen to afford [$\mathbf{L}^{\mathbf{SPh}}Cu^{II}$-$\eta^2$-$O_2^{\bullet-}$]OTf/[$\mathbf{L}^{\mathbf{Se}}Cu^{II}$-$\eta^2$-$O_2^{\bullet-}$]OTf that feature a superoxo ligand bound in a side-on manner;[31] these species react with 9,10-DHA in a Hydrogen Atom Transfer (HAT) reaction, *i.e.* a one electron reaction process, although differences in reactivity are evidenced in the presence of a large excess of DHA between

the thio- and selenoether based systems. ^{77}Se NMR spectroscopic data allow us to postulate that the selenoether ligand is bound at room temperature, but dissociation of the selenoether moiety upon reaction with O_2 is supported by DFT calculations, both in the putative cupric superoxo complex, and, as indicated by EPR, in the cupric hydroperoxo that results after initial HAT. Thus, the combined experimental and theoretical evidence point at reactive $[LCu^{II}\text{-}\eta^2\text{-}O_2^{\bullet-}]^+$ species as electrophilic centers that are poised for C-H activation after decoordination of the chalcogen ethers. These observations may be extended to the thioether analogues in synthetic systems, and to related copper monooxygenases that feature methionine residues coordinated to the Cu centers. Despite the similarities, care must be exercised when replacing S with Se in related systems, since this may influence the HAT capability of the resulting copper-oxygen species. This cautionary note notwithstanding, the overall observations hint at hemilability as a potential tool in nature's repertoire to tune metalloenzymatic active sites that merits further scrutiny.

Experimental Section

General. Air-sensitive compounds were manipulated under an atmosphere of dinitrogen in a glovebox or by vacuum-line and Schlenk techniques. Solvents were dried by standard methods and distilled under N_2 prior to use. $Cu(H_2O)_6(CF_3SO_3)_2$, $[Cu(CH_3CN)_4]CF_3SO_3$, $NBu_4(CH_3SO_3)$, cysteamine hydrochloride, 2-iodoethylbenzene, potassium hydroxide, diphenyl diselenide, 2-bromoethylamine hydrobromide, $NaBH_4$, and 9,10-dihydroanthracene (9,10-DHA) were used as received from Aldrich Chemical Co. 9,10-DHA-d_4 was prepared per literature procedures.[59] $Cu(H_2O)_6(OMes)_2$ was prepared from $CuCO_3$ by addition of 2 equivs. HOMes (Mes = CH_3SO_2) in water.

Instrumental. Low temperature UV–visible experiments were carried out with an Agilent spectrophotometer model 8453 equipped with a liquid nitrogen chilled Unisoku USP-203-A cryostat using a 1 cm modified Schlenk cuvette. Melting points were determined on an Electrothermal Mel-Temp apparatus and are uncorrected. Infrared spectra were recorded with a Bruker Tensor 27 spectrophotometer in the 4000–400 cm^{-1} region as KBr disks. NMR spectra were recorded on a JEOL Eclipse 300 spectrometer in $CDCl_3$ with tetramethylsilane as an internal standard, or in CD_3CN referenced relative to the residual solvent protons at 300 (^{1}H) or 75 MHz (^{13}C), or on a Bruker Avance III at 400 MHz for variable temperature ^{1}H NMR measurements and Bruker Avance III HD at 500 MHz. Mass spectra were obtained on a JEOL JMS-AX505HA spectrometer (Electron Ionization), or a Bruker Daltonics Esquire 6000 spectrometer with an ion trap (Electrospray). Elemental analyses were performed at the microanalytical facility of the Instituto de Química, UNAM. GC-MS determinations were performed using an Agilent 5975C instrument equipped with a 30 m DB-5MS capillary (0.32 mm i.d.) column in CH_2Cl_2. Electron paramagnetic resonance measurements were performed using a conventional Bruker EMX spectrometer operating in the X band (about 9.39 GHz). The temperature was controlled using an Oxford ITC and ESR900 cryostat. The low-temperature measurements were performed using a cryogen-free Stinger system from ColdEdge that permits reaching 7 K as a base temperature. EPR spectra were simulated using the EasySpin toolbox developed for MATLAB.[60] The optimum Hamiltonian parameters were obtained using the 2nd order perturbation, then an exact diagonalization was used for the final simulations. The Hamiltonian used for the simulations is the following equation:

$$H = \mu_B S[g]B + S[A_{Cu}]I_{Cu} \qquad (1)$$

X-Ray crystallography. Single crystals were mounted on an Oxford Diffraction Gemini Atlas diffractometer with a CCD area detector; the radiation using a monochromator of graphite with λMoKα = 0.71073 Å, at 130 K. Unit cell parameters were determined with a set of three runs of 15 frames (1° in ω). The double pass method of scanning was used to exclude any noise. The collected frames were integrated by using an orientation matrix determined from the narrow frame scans. CRYSALISPRO and CRYSALIS RED software packages for data collection and data integration with the latter.[61] Analysis of the integrated data did not reveal any decay. Collected data were corrected for absorption effects by an analytical numeric absorption correction[62] using a multifaceted crystal model based on expressions upon the Laue symmetry with equivalent reflections. For [**L**^{SPh}CuCl]OTf, the diffraction data were collected on a Bruker Smart APEX 3 diffractometer with a CCD area detector, with radiation source of λMoKα = 0.71073 Å at 150 K, using APEX 3 software packages[63] for data collection and data integration. All structures solution and refinement were carried out with SHELXS-2014[64] and SHELXL-2014,[65] respectively. WinGX v2021[66] was used to prepare material for publication. Full-matrix least-squares refinement was carried out by minimizing $(Fo^2 - Fc^2)^2$. All nonhydrogen atoms were refined anisotropically. For the H atoms on water molecules (H–O), they were located in a difference map and refined isotropically with $U_{iso}(H) = 1.5$ for H–O. Hydrogen atoms attached to carbon atoms were placed in geometrically idealized positions and refined as riding on their parent atoms, with C—H = 0.95 – 0.99 Å with $U_{iso}(H) = 1.2\ U_{eq}(C)$ for aromatic and methylene groups, and $U_{iso}(H) = 1.5\ U_{eq}(C)$ for methyl group. In [**L**^{SPh}Cu]$_2$(OTf)$_2$, the triflate anion and THF molecules are disordered. X-ray data for [**L**^{SPh}Cu(NO$_3$)]OTf were collected on an Oxford diffraction Eos Diffractometer (graphite monochromated Mo-Kα radiation, λ = 0.71073 Å) at ambient temperature. Data reduction and corrections for absorption was performed using CrysAlisPro. The structure was solved by charge flipping as implemented in Super flip[67] and refined against F in JANA200.[68] All non-hydrogen atoms were identified from electron density maps while the positions and displacement parameters for hydrogen were generated from geometrical constrains in a riding model. The refinement proceeded smoothly to satisfactory agreement

parameters and a featureless electron density map. Final agreement parameters converged to wR/R for observed reflections of 0.051/0.049 and a goodness-of-fit of 1.18. Crystal data and experimental details of the structure determination are listed in Table S1. Crystallographic data have been deposited at the Cambridge Crystallographic Data Center as supplementary materials CCDC: 2328169-2328171 and 2330844. Copies of the data can be obtained free of charge on application to CCDC, 12 Union Road, Cambridge CB2 1EZ, UK. e-mail: deposit@ccdc.cam.ac.uk.

Computational Details. DFT calculations were performed using the ORCA program package.[69,70] Geometry optimizations were carried out using the GGA functional BP86[71,72] with the def2-TZVP basis sets.[73] For the Coulomb fitting the def2/J auxiliary basis sets were used.[74] Increased angular and radial integration grids (Grid4 and IntAcc 6.0, respectively, in Orca convention) and tight SCF convergence criteria were employed. Slow SCF convergence settings were applied in combination with recalculation of the full Fock matrix for each SCF step (DirectResetFreq 1). To resemble the experimental conditions as closely as possible, all calculations including geometry optimizations were performed in acetonitrile solvent by invoking the Control of the Conductor-like Polarizable Continuum Model (CPCM).[75] To ensure that the resulting structures converged to a local minimum on the potential energy surface, frequency calculations were performed and resulted in only positive normal vibrations. The Gibbs free energies were computed from the optimized structures as a sum of electronic energy, solvation, and thermal corrections to the free energy. Redox potentials were obtained from the calculated free energy change between oxidized and reduced species in solution. They are relative potentials referenced to the ferrocene couple and, as such, a computed value of 5.125 eV was subtracted to make direct comparisons to experimental data.[76] Electronic structures were obtained from single-point DFT calculations using the hybrid functional B3LYP[77,78] together with the def2-TZVP basis set.[73] EPR calculations, namely g-tensors, were obtained from single-point calculations using a modified version of B3PW91[77,79] with 40% exact (Hartree–Fock) exchange.[80] The large aug-cc-pVTZ-Jmod basis set[81] was applied for the metal center while the def2-TZVP basis sets[73] were used for all other atoms. Hyperfine tensors were obtained from single-point calculations using the B3PW91[77,79] functional together with the aug-cc-pVTZ-Jmod basis set[81] for the metal center and the def2-TZVP basis sets[73] for all other atoms. UV-vis spectral features were predicted using TD-DFT using the hybrid functional B3LYP[77,78] and the def2-TZVP basis sets.[73] Vertical electronic transitions were calculated using simplified time-dependent DFT within the Tamm-Dancoff approximation (TDA).[82-86] To increase computational efficiency, the RI approximation[87] was used in calculating the Coulomb term, and at least 70 excited states were calculated in each case. Spin density plots, molecular orbitals as well as difference density plots for each transition were generated using the ORCA plot utility program and were visualized with the Chemcraft program (http://chemcraftprog.com).

Synthesis of amines

2-phenylethylthioethylamine (ASPh). In a 100 mL round bottom flask, 1.00 g (7.6 mmol) of cysteamine hydrochloride was dissolved in 20 mL of distilled ethanol and 0.97 g (17 mmol) of KOH were added to the solution. The mixture was stirred at room temperature for 1 h, after this time 1.77g (7.6 mmol) of (2-iodoethyl)benzene was added dropwise at 0°C; the mixture was then heated to reflux for 3 h. The ethanolic solution was evaporated under reduced pressure, and the resulting tan oil was extracted with CH_2Cl_2. Yield: 88% (1.7 g). M.p.112-114 °C. IR (ATR): ν = 3348, 3082, 3059, 3026, 2916, 2851, 1600, 1494, 1451, 1381, 1318, 1271, 1225, 1122, 1071, 1027, 888, 746, 697, 562, 490 cm^{-1}. DART MS: $C_6H_5CH_2CH_2SCH_2CH_2$ = 165 *m/z*; ASPh = 182 *m/z*. ^1H NMR ($CDCl_3$, 300 MHz, 20°C); δ: 2.72 (t, 2 H, CH_2S), 2.79 (t, 2 H, CH_2N), 2.95 (m, 4 H, $CH_2CH_2C_6H_5$), 3.17 (s, 2 H, NH_2), 7.24 (m, 3 H, C_6H_5), 7.32 (m, 2 H, C_6H_5) ppm. Elemental Analysis Calculated for $C_{10}H_{18}ClNOS$: C, 50.94; H, 7.70; N, 5.94; S, 13.60; Found: C, 49.27; H, 5.06; N, 5.14; S, 9.58.

2-phenylselenoethylamine (ASe). In a 100 mL round bottom flask, 1.00 g (3.20 mmol) of diphenyl diselenide was dissolved in 20 mL of distilled ethanol and NaBH4 was added until decoloration of the solution was observed. In a Schlenk flask, 1.31 g (6.40 mmol) of (2-bromoethyl)amine was dissolved in 10 mL of distilled ethanol and 0.15 g (6.40 mmol) of Na was added to this mixture; once this reaction mixture was colorless, it was added through a cannula into the senelolate solution. The mixture was heated to reflux while stirring for 3 h. The ethanolic solution was filtrated and acidified with 1 equiv. of HCl 1M to isolate the hydrochloride of the amine. Yield: 53% (0.81 g). M.p.: > 300°C (dec. 300–305°C). IR (ATR): ν = 3623, 3545, 3383, 3216, 1616, 1412, 1327, 1281, 1220, 1101, 1030, 919, 782, 746, 689, 675, 552, 492, 467, 435 cm^{-1}. DART-MS: ASe = 201 *m/z*. ^1H NMR ($CDCl_3$, 300 MHz, 20°C) δ: 1.89 (s, 2H, NH_2), 2.98 (m, 4 H, $CH_2CH_2NH_2$), 7.27 (m, 3 H, C_6H_5), 7.52 (m, 2 H, C_6H_5) ppm. ^{77}Se NMR (THF-d_8, 57 MHz, 20°C) δ: 256.34 ppm.

Synthesis of ligands

[bis(1-methyl-2 methylbenzimidazolyl)(phenylethyltioethyl)amine] (L^{SPh}). In a 100 mL round flask, 500 mg (2.80 mmol) of 1-methyl-2-chloromethylbenzimidazole, 382 mg (2.78 mmol) of K_2CO_3 and 40 mg (0.27 mmol) of NaI were dissolved in CH_3CN, the reaction mixture was stirred at room temperature for 3 h; then 251 mg (1.39 mmol) of ASPh was added. The mixture was heated to reflux for 3 h. After cooling to room temperature, the solution

was filtered and volatiles were evaporated under reduced pressure, the concentrated solution was evaporated slowly to afford pale yellow crystals. Yield: 55% (0.298 g). M.p.: 127-130 °C. IR (KBr): ν = 3057, 3028, 2922, 2807, 1611, 1511, 1475, 1454, 1437, 1398, 1358, 1330, 1289, 1234, 1206, 1173, 1147, 1121, 1097, 1029, 988, 939, 906, 860, 798, 762, 741, 696, 653, 569, 538, 499, 471, 440, 410 cm^{-1}. DART-MS: $\mathbf{L^{SPh}}$ = 470 *m/z*. ^{1}H NMR ($CDCl_3$, 300 MHz, 20°C) δ = 2.72 (t, CH_2-S), 2.79 (t, CH_2-N), 2.95 (m, $CH_2CH_2C_6H_5$), 3.17 (s, NH_2), 7.24 (m, C_6H_5), 7.32 (m,C_6H_5) ppm. ^{13}C{^{1}H} NMR ($CDCl_3$, 75 MHz, 20°C): δ = 151.0 (Bzim), 142.0 (Bzim),140.2 (Bzim), 136.0 (C_6H_5), 128.4 (C_6H_5), 128.3 (C_6H_5), 126.2 (C_6H_5), 122.8 (Bzim), 122.1 (Bzim), 119.7 (Bzim), 119.1 (Bzim), 54.02 (S-CH_2), 51.39 (N-CH_2), 36.11 (NCH_2Bzim), 33.34 (NCH_3), 29.91 (CH_2), 29.75 (CH_2) ppm. $E_{1/2}$ = -190 mV (Fc^+/Fc).

[bis(1-methyl-2 methylbenzimidazolyl)(phenylethyltioethyl)amine] ($\mathbf{L^{Se}}$). In a 100 mL round flask, 500 mg (2.8 mmol) of 1-methyl-2-chloromethylbenzimidazole, 382 mg (2.78 mmol) of K_2CO_3 and 40 mg (0.27 mmol) of NaI were dissolved in CH_3CN, and the mixture was stirred at room temperature for 3 h; then 280 mg (1.38 mmol) of ASe was added. The mixture was heated to reflux for 3 h. After cooling to room temperature, the solution was filtered, and volatiles were evaporated under reduced pressure to obtain an orange microcrystalline material. Yield: 89% (0.515 g). M. p.: 112–115 °C. IR (KBr): ν = 3049, 2927, 2847, 1699, 1671, 1612, 1577, 1509, 1473, 1436, 1397, 1360, 1329, 1284, 1257, 1234, 1176, 1153, 1122, 1077, 1022, 1001, 959, 929, 904, 848, 733, 689, 666, 576, 536, 462, 439 cm^{-1}. DART MS: $\mathbf{L^{Se}}$ = 490 *m/z*. ^{1}H NMR (THF-d_8, 300 MHz, 20°C) δ: 3.04 (t, 2 H, CH_2-S), 3.11(t, 2 H CH_2-N), 3.70 (s, 6 H, NMeBzim), 4.05 (s, 4 H, NCH_2), 7.02 (m, 4 H, Bzim), 7.19 (m, 5 H, C_6H_5-Se), 7.34 (dd, 2 H, Bzim), 7.59 (dd, 2 H, Bzim) ppm. ^{13}C{^{1}H} NMR (THF-d_8, 75 MHz, 20 °C): δ = 152.3 (Bzim), 143.9 (Bzim),137.5 (Bzim), 132.4 (Se-C_6H_5), 131 (Se-C_6H_5), 129.6 (Se-C_6H_5),127 (Se-C_6H_5), 122.9 (Bzim), 122.1 (Bzim), 120.4 (Bzim), 110 (Bzim), 55.19 (Se-CH_2), 51.33 (N-CH_2), 30.16 (NCH_2Bzim), 30.11 (NCH_3) ppm. ^{77}Se NMR (THF-d_8, 57 MHz, 20°C) δ = 273.93 ppm. $E_{1/2}$ = -131 mV (Fc^+/Fc).

Synthesis of complexes

[$\mathbf{L^{SPh}}$Cu]OTf. 50 mg (0.10 mmol) of $\mathbf{L^{SPh}}$ and 40 mg (0.10 mmol) of [$Cu(CH_3CN)_4$]OTf were charged in a Schlenk flask inside of the glovebox, and dissolved in anhydrous acetonitrile; the mixture was stirred for 3 h under N_2 atmosphere, and then concentrated under reduced pressure on a vacuum line. The resulting yellow solid was washed with diethyl ether and dried under vacuum to afford the desired solid. Yield: 47 % (0.034 g). M.p.: 165-167 °C; ^{1}H NMR (300 MHz, 20°C, [D_8]THF): δ = 2.60 (t, 2 H, CH_2-S), 2.85 (t, 2 H, CH_2-N), 2.93 (m, 4 H, CH_2CH_2-Ph), 3.56 (s, 2 H, NH_2) 7.01 (m, 4 H, Bzim), 7.1 (m, 3 H, Ph), 7.14 (m, 2 H, Ph), 7.22 (dd, 2 H, Bzim), 7.87 (dd, 2 H, Bzim) ppm; IR (KBr): ν = 3054, 2937, 1613, 1577, 1480, 1448, 1329, 1257, 1149, 1101, 1028, 867, 801, 739, 691, 636, 572, 517, 465, 432 cm^{-1}; elemental analysis calcd (%) for [$\mathbf{L^{SPh}}$Cu]OTf: C, 51.05; H, 4.58; N, 10.27; found: C, 50.82; H, 4.84; N, 9.93.

[$\mathbf{L^{Se}}$Cu]OTf. 50 mg (0.10 mmol) of $\mathbf{L^{Se}}$ and 39 mg (0.10 mmol) of [$Cu(CH_3CN)_4$]OTf were charged in a Schlenk flask inside a glovebox, and dissolved in anhydrous THF; the mixture was stirred for 3 h under N_2 atmosphere, and then concentrated under reduced pressure on a vacuum line. The resulting colorless solid was washed with diethyl ether and dried under vacuum to afford an off-white solid. Yield: 45% (0.032 g). M.p.: 111-113 °C; ^{1}H NMR (300 MHz, 20°C, [D_8]THF): δ = 3.04 (t, 2 H, CH_2-S), 3.11 (t, 2 H CH_2-N), 3.70 (s, 6 H, NMeBzim), 4.70 (s, 4 H, NCH_2), 7.02 (m, 4 H, Bzim), 7.19 (m, 5 H, C_6H_5-Se), 7.34 (dd, 2 H, Bzim), 7.59 (dd, 2 H, Bzim) ppm; ^{77}Se NMR (THF-d_8, 57 MHz, 20°C, [D_8]THF): δ = 223 ppm; IR (KBr): ν = 3473, 3058, 2946, 2873, 1596, 1576, 1481, 1451, 1327, 1256, 1222, 1148, 1064, 1027, 964, 922, 886, 739, 690, 634, 571, 515, 465, 433 cm^{-1}; elemental analysis calcd (%) for [$\mathbf{L^{Se}}$Cu]OTf: C, 46.26; H, 3.88; N, 9.99; Found: C, 45.80; H, 4.24; N, 9.60.

[$\mathbf{L^{SPh}}$CuCl]OTf. In a 100 mL round flask 50 mg (0.11 mmol) of $\mathbf{L^{SPh}}$ were mixed with an equimolar amount of $Cu(OTf)_2$ (39 mg, 0.11 mmol), dissolved in CH_3CN, and stirred for 3 h at room temperature; after evaporation of volatiles under vacuum, the green solid obtained was washed with diethyl ether, and dried under reduced pressure. Yield: 92% (0.07 g). M.p.: 242-245 °C; IR (KBr): ν = 3415, 3052, 2955, 2924, 2829, 1645, 1616, 1565, 1504, 1452, 1357, 1326, 1222, 1156, 1100, 1025, 935, 886, 860, 795, 745, 724, 700, 633, 572, 514, 490 cm^{-1}; UV-vis (0.3 mM, THF, rt): λ = 343 nm S→Cu(II), ε = 2201 $M^{-1}cm^{-1}$, λ = 634 nm *d-d*, ε = 81 $M^{-1}cm^{-1}$; EPR (77 K, CH_3CN): $g_{\|}$ = 2.257; $g_{\perp}$ = 2.071; $A_{\|}$ = 164 G; elemental analysis calcd (%) for [$\mathbf{L^{SPh}}$CuCl)$(H_2O)_3$]OTf: C, 45.13; H, 4.83; N, 9.07; S, 8.31; Found: C, 45.35; H, 4.86; N, 8.94; S, 8.31.

[$\mathbf{L^{Se}}$Cu(H_2O)]$(OTf)_2(H_2O)_2$. In a 100 mL round flask 52 mg of $\mathbf{L^{Se}}$ (0.11 mmol) and 39 mg of $Cu(OTf)_2$ (0.11 mmol) were dissolved in 20 mL of CH_3CN. The green solution was stirred for 3 h; after this time the acetonitrile was evaporated and the green solid was washed with diethyl ether, affording the desired product. The complex [($\mathbf{L^{Se}}$Cu(H_2O)]$(OMes)_2(H_2O)_4$ was prepared in an analogous fashion. [$\mathbf{L^{Se}}$Cu(H_2O)]$(OTf)_2(H_2O)_2$: Yield 98% (0.09 g). M.p.: 115 – 117°C; IR (KBr): ν = 3208, 2956, 2929, 1649, 1617, 1503, 1482, 1456, 1324, 1274, 1222, 1156, 1025, 935, 913, 743, 690, 633, 572, 514, 464, 431 cm^{-1}; UV-vis (0.3 mM, THF, rt) λ = 344 nm, ε = 1167 $M^{-1}cm^{-1}$ Se→Cu(II), λ = 689 nm *d-d*, ε = 101 $M^{-1}cm^{-1}$; EPR (77 K, CH_3CN) $g_{\|}$ = 2.283, $g_{\perp}$ = 2.069 and $A_{\|}$ = 157 G; elemental analysis calcd (%) for [$\mathbf{L^{Se}}$Cu(H_2O)]$(OTf)_2(H_2O)_2$: C, 37.19; H, 3.68; N, 7.75; S, 7.09; Found: C, 36.95; H, 3.37; N, 7.06; S, 7.33. [$\mathbf{L^{Se}}$Cu(H_2O)]$(OMes)_2(H_2O)_4$: Yield 88% (0.07 g); elemental

analysis calcd (%) for $[L^{Se}Cu(H_2O)](OMes)_2(H_2O)_4$: C, 40.41; H, 5.21; N, 8.41; S, 7.70; Found: C, 40.41; H, 5.18; N, 7.76; S, 7.63.

Reactivity studies

Generation of $[(L^{SPh}/L^{Se})Cu^{II}O_2^{\bullet-}]^+$. From a 1 mM stock solution, 0.3 mM of Cu^I complex solutions were prepared in 10 mL of THF inside a glovebox. 4 mL of the diluted solution was transferred into a 1 cm Schlenk cuvette, which was sealed with a rubber septum. The cell was transferred to the pre-cooled cryostat and chilled at –80°C with 10 minutes allowed for equilibration prior to oxygenation. Dioxygen was gently bubbled using a long needle for 40 seconds, forming $[(L^{SPh}/L^{Se})Cu^{II}O_2^{\bullet-}]^+$. $[L^{SPh}Cu^{II}O_2^{\bullet-}]^+$. UV-vis (-80°C, THF): λ = 336 nm ε = 1905 M^{-1} cm^{-1}. $[L^{Se}Cu^{2+}O_2^{\bullet-}]^+$. UV-vis (-80°C, THF): λ = 336 nm, ε = 1772 M^{-1} cm^{-1}.

Generation of $[(L^{SPh}/L^{Se})Cu^{II}OOH]^+/[(L^{SPh}/L^{Se})_2Cu^{II}_2$-$\mu$–$\eta^2$:$\eta^2$-$O_2]^{2+}$ mixture. 0.3 mM Cu^{II} complex solutions were prepared in THF inside a glovebox. 4 mL of the diluted solution was transferred into a 1 cm Schlenk cuvette, which was sealed with a rubber septum. The cell was transferred to the pre-cooled cryostat and chilled at –60°C with 10 minutes allowed for equilibration prior to oxygenation. Then, 10 equivs. of a 1:1 H_2O_2/NEt_3 mixture were added via microsyringe (45 μL), and the reaction analyzed by UV-vis for 60 min.

Model substrate activation by cupric complexes

$[(L^{SPh}/L^{Se})Cu^{II}O_2^{\bullet-}]^+$ complexes. Once the cupric superoxo complexes were generated at low temperature, 10-100 equivs. of 9,10-dihydroanthracene (9,10-DHA) were added in 0.3 mM THF solutions. The reaction was monitored by UV-vis spectroscopy for 1 h, the observed decrease in the charge transfer band was associated with the consumption of the cupric superoxo complex. After 2 h, the reaction was stopped and liquid-liquid extraction with CH_2Cl_2 and an aqueous solution of Na_2EDTA were made, the organic phase was analyzed by gas chromatography coupled to mass spectrometry (GC-MS).

Supporting Information

Additional electrochemical and spectroscopic data, selected X-ray crystal structural and DFT data. This material is available free of charge via the Internet. The following files are available free of charge: spectroscopic data and calculations (PDF), crystallographic data (cif).

Author Contributions. The manuscript was written through contributions of all authors. All authors have given approval to the final version of the manuscript.

Funding Sources. CONAHCyT (Becas 254496 and 748137), the Swedish Research Council (the Swedish Research Links program), ECOS Nord (291247), and DGAPA-PAPIIT (IN210214 and IN203317), and IR INFRANALYTICS FR2054.

Acknowledgements

The authors thank Carmen Márquez, Eréndira García and Lucero Ríos for mass spectrometry measurements, María de la Paz Orta for combustion analysis, Rocío Patiño† for IR, Beatriz Quiroz and Ruben Gaviño for NMR experiments, Virginia Gómez-Vidales for EPR determinations, and Claude Arnold for assistance and management of computer resources.

Keywords: Copper • Monooxygenase • Hemilabile • C-H activation • DFT calculations

[1] D. Robertson, V. Haile, S. E. Perry, R. M. Robertson, J. A. Phillips, I. Biaggioni, *Hypertension* **1991**, *18*, 1.

[2] G. P. Mueller, W. J. Driscoll, B. A. Eipper, *J. Pharmacol. Exp. Ther*. **1999**, *290*, 1331.

[3] J. P. Klinman, *Chem. Rev*. **1996**, *96*, 2541.

[4] C. P. Cubells, J. F. Zabetian, *Psychopharmacology* **2004**, *174*, 463.

[5] T. V. Vendelboe, P. Harris. Y. Zhao, T. S. Walter, K. Harlos, K. E. Omari, H. E. M. Christensen, *Sci. Adv*. **2016**, *2*, e1500980.

[6] B. A. Eipper, S. L. Milgram, E. J. Husten, H. Yun, R. E. Mains, *Protein Sci*. **1993**, *2*, 489.

[7] F. N. Bolkenius, A. J. Ganzhorn, *Gen. Pharmac*. **1998**, *31*, 655.

[8] T. C. Owen, D. J. Merkler, *Med. Hypotheses* **2004**, *62*, 392.

[9] N. Jiang, A. S. Kolhekar, P. S. Jacobs, R. E. Mains, B. A. Eipper, P. H. Taghert, *Dev. Biol*. **2000**, *226*, 118.

[10] a) J. P. Klinman, *J. Biol. Chem*. **2006**, *281*, 3013; b) J. P. Evans, K. Ahn, J. P. Klinman, *J. Biol. Chem*. **2003**, *278*, 49691.

[11] A. Crespo, M. A. Martí, A. E. Roitberg, L. M. Amzel, D. A. Estrin, *J. Am. Chem. Soc*. **2006**, *128*, 12817.

[12] a) T. Kamachi, N. Kihara, Y. Shiota, K. Yoshizawa, *Inorg. Chem*. **2005**, *44*, 4226; b) K. Yoshizawa, N. Kihara, T. Kamachi, Y. Shiota, *Inorg. Chem*. **2006**, *45*, 3034.

[13] a) I. Blain, M. Pierrot, M. Giorgi, M. Réglier, *Acad. Sci. Paris, Série IIc* **2001**, *4*, 1; b) A. Amine, Z. Atmani, A. El Hallaoui, M. Giorgi, M. Pierrot, M. Réglier, *Bioorg. Med. Chem. Lett.* **2002**, *12*, 57.

[14] S. T. Prigge, B. A. Eipper, R. E. Mains, L. M. Amzel, *Science* **2004**, *304*, 864.

[15] T. Hoppe, P. Josephs, N. Kempf, C. Wölper, S. Schindler, A. Neuba, G. Henkel, *Z. Anorg. Allg. Chem*. **2013**, *639*, 1504.

[16] J. S. Woertink, L. Tian, D. Maiti, H. R. Lucas, R. A. Himes, K. D. Karlin, F. Neese, C. Würtele, M. C. Holthausen, E. Bill, J. Sundermeyer, S. Schindler, E. I. Solomon, *Inorg Chem*. **2010**, *49*, 9450.

[17] N. W. Aboelella, B. F. Gherman, L. M. R. Hill, J. T. York, N. Holm, V. G. Young, C. J. Cramer, W. B. Tolman, *J. Am. Chem. Soc*. **2006**, *128*, 3445.

[18] C. J. Cramer, W. B. Tolman, *Acc. Chem. Res*. **2007**, *40*, 601.

[19] T. Tano, Y. Okubo, A. Kunishita, M. Kubo, H. Sugimoto, N. Fujieda, T. Ogura, S. Itoh, *Inorg Chem*. **2013**, *52*, 10431.

[20] Q. ZhuY. LianS. Thyagarajan, S. E. Rokita, K. D. Karlin, N. V. Blough, *J. Am. Chem. Soc.* **2008**, *130*, 6304.

[21] a) S. Kim, J. Y. Lee, R. E. Cowley, J. W. Ginsbach, M. A. Siegler, E. I. Solomon, K. D. Karlin, *J. Am. Chem. Soc*. **2015**, *137*, 2796; b) M. Bhadra, W. J. Transue, H. Lim, R. E. Cowley, J. Y. C. Lee, M. A. Siegler, P. Josephs, G. Henkel, M. Lerch, S. Schindler, A. Neuba, K. O. Hodgson, B. Hedman, E. I. Solomon, K. D. Karlin, *J. Am. Chem. Soc*. **2021**, *143*, 3707.

[22] I. Castillo, V. M. Ugalde-Saldívar, L. A. Rodríguez-Solano, B. N. Sánchez-Eguía, E. Zeglio, E. Nordlander, *Dalton Trans*. **2012**, *41*, 9394.

[23] I. Castillo, B. N. Sánchez-Eguía, P. R. Martínez-Alanis, V. M. Ugalde-Saldívar, M. Flores-Alamo, *Polyhedron* **2015**, *85*, 824.

[24] K. Fujisawa, M. Tanaka, Y. Moro-oka, N. Kitajima, *J. Am. Chem. Soc*. **1994**, *116*, 12079.

[25] M. Kodera, T. Kita, I. Miura, N. Nakayama, K. Kano, S. Hirota, *J. Am. Chem. Soc*. **2001**, *123*, 7715.

[26] D.-H. Lee, L. Q. Hatcher, M. A. Vance, R. Sarangi, A. E. Milligan, A. A. Narducci Sarjeant, C. D. Incarvito, A. L. Rheingold, K. O. Hodgson, B. Hedman, E. I. Solomon, K. D. Karlin, *Inorg. Chem*. **2007**, *46*, 6056.

[27] A. Kunishita, M. Kubo, H. Sugimoto, T. Ogura, K. Sato, T. Takui, S. Itoh, *J. Am. Chem. Soc.* **2009**, *131*, 2788.

[28] C. Würtele, K. H. Gaoutchenova, M. C. Holthausen, J. Sundermeyer, S. Schindler, *Angew. Chem. Int. Ed.* **2006**, *45*, 3867-3869.

[29] C. E. Elwell, N. L. Gagnon, B. D. Neisen, D. Dhar, A. D. Spaeth, G. M. Yee, W. B. Tolman, *Chem. Rev*. **2017**, *117*, 2059-2107

[30] P. J. Donoghue, A. K. Gupta, D. W. Boyce, C. J. Cramer, W. B. Tolman, *J. Am. Chem. Soc*. **2010**, *132*, 15869-15871.

[31] B. N. Sánchez-Eguía, M. Flores-Alamo, M. Orio, I. Castillo, *Chem. Commun*. **2015**, *51*, 11134-11137.

[32] S. Itoh, *Acc. Chem. Res*. **2015**, *48*, 2066-2074.

[33] H. Duddeck, in *Progress in NMR Spectroscopy*, *Vol. 27* (Ed.: D. Neuhaus), Elsevier, Great Britain, **1995**, pp. 1-323.

[34] A. Böck, K. Forchhammer, J. Heider, W. Leinfelder, G. Sawers, B. Veprek, F. Zinoni, *Mol. Microbiol.* **1991**, *5*, 515-520.

[35] W. Levason, S. D. Orchard, G. Reid, *Coord. Chem. Rev*. **2002**, *225*, 159-199.

[36] M. M. Kimani, D. Watts, L. A. Graham, D. Rabinovich, G. P. A. Yap, J. L. Brumaghim, *Dalton Trans.* **2015**, *44*, 16313-16324.

[37] M. J. Kimani, J. L. Brumaghim, D. VanDerveer, *Inorg. Chem.* **2010**, *49*, 9200-9211.

[38] K. B. Alwan, E. F. Welch, R. J. Arias, B. F. Gambill, N. J. Blackburn, *Biochemistry* **2019**, *58*, 3097−3108.

[39] K. B. Alwan, E. F. Welch, N. J. Blackburn, *Biochemistry* **2019**, *58*, 4436-4446.

[40] K. W. Rush, K. A. S. Eastman, E. F. Welch, V. Bandarian, N. J. Blackburn, *J. Am. Chem. Soc*. **2024**, *146*, 5074-5080.

[41] S. Ghosh, G. P. Tochtrop, *Tetrahedron Lett*. **2009**, *50*, 1723-1726.

[42] S. V. Amosova, N. A. Makhaeva, A. V. Martynov, V. A. Potapov, B. R. Steele, I. D. Kostas, *Synthesis* **2005**, *10*, 1641-1648.

[43] Q. Chen, S. Xu, X. Lu, M. V. Boeri, Y. Pepelyayeva, E. L. Diaz, S.-D. Soni, M. Allaire, M. B. Forstner, B. J. Bahnson, S. Rozovsky, *J. Phys. Chem. B* **2020**, *124*, 601-616.

[44] R. Kumar, D. G. Tuck, *Can. J. Chem*. **1989**, *67*, 127-219.

[45] W. Li, G. Kagan, R. Hopson, P. G. Williard, *J. Chem. Educ*. **2011**, *88*, 1331-1335.

[46] A. W. Addison, M. Carpenter, L. K.-M. Lau, M. Wicholas, *Inorg. Chem*. **1978**, *17*, 1545-1552.

[47] M. Łabanowska, E. Bidzínska, A. Para, M. Kurdziel, *Carbohydr. Polym*. **2012**, *87*, 2605-2613.

[48] L. Yang, D. R. Powell, R. P. Houser, *Dalton Trans*. **2007**, *9*, 955-964.

[49] A. W. Addison, T. N. Rao, J. Reedijk, J. Van Rijn, G. C. Verschoor, *J. Chem. Soc., Dalton Trans*. **1984**, 1349-1356.

[50] D. G. Vargas-Pineda, T. Guardado, F. Cervantes-Lee, A. J. Metta-Magana, K. H. Panell, *Inorg. Chem*. **2010**, *49*, 960-968.

[51] P. Chen, J. Bell, B. A. Eipper, E. I. Solomon, *Biochemistry* **2004**, *43*, 5735−5747.

[52] X. Ottenwaelder, D. J. Rudd, M. C. Corbett, K. O. Hodgson, B. Hedman, T. D. P. Stack, *J. Am. Chem. Soc*. **2006**, *128*, 9268-9269.

[53] C. Citek, S. Herres-Pawlis, T. D. P. Stack, *Acc. Chem. Res*. **2015**, *48*, 2424-2433.

[54] R. Cao, C. Saracini, J. W. Ginsbach, M. T. Kiebber-Emmons, M. A. Siegler, E. I. Solomon, S. Fukuzumi, K. D. Karlin, *J. Am. Chem. Soc*. **2016**, *138*, 7055-7066.

[55] A. Conde, L. Vilella, D. Balcell, M. M. Díaz-Requejo, A. Lledós, P. J. Pérez, *J. Am. Chem. Soc*. **2013**, *135*, 3887-3896.

[56] E. F. Welch, K. W. Rush, R. J. Arias, N. J. Blackburn, *J. Inorg. Biochem*. **2022**, *231*, 111780.

[57] P. Wu, F. Fan, J. Song, W. Peng, J. Liu, C. Li, Z. Cao, B. Wang, *J. Am. Chem. Soc*. **2019**, *141*, 19776-19789.

[58] S. Maheshwari, C. Shimokawa, K. Rudzka, C. D. Kline, B. A. Eipper, E. E. Mains, S. B. Gabelli, N. Blackburn, L. M. Amzel, *Commun. Biol*. **2018**, *1*, 74.

[59] C. R. Goldsmith, T. T. Jonas, T. D. P. Stack, *J. Am. Chem. Soc*. **2002**, *124*, 83-96.

[60] S. Stoll, A. Schweiger, *J. Magn. Reson*. **2006**, *178*, 42-55.

[61] Agilent CrysAlis PRO and CrysAlis RED, Agilent Technologies, Yarnton (England), **2013**.

[62] R. C. Clark, J. S. Reid, *Acta Cryst*. **1995**, *A51*, 887-897.

[63] APEX2 Software Package, Bruker AXS Inc., Madison (USA), **2005**.

[64] G. M. Sheldrick, *Acta Cryst*. **2015**, *A71*, 3-8.

[65] G. M. Sheldrick, *Acta Cryst*. **2015**, *C71*, 3-8.

[66] L. J. Farrugia, *J. Appl. Cryst*. **2012**, *45*, 849-854.

[67] L. Palatinus, G. Chapuis, *J. Appl. Cryst*. **2007**, *40*, 786-790.

[68] a) V. Petricek, M. Dusek, L. Palatinus, *Crystallographic computing system Jana2006*, De Gruyter, Berlin, **2006**; b) V. Petricek, M. Dusek, L. Palatinus, *Z. Kristallogr*. **2014**, *229*, 345-352.

[69] F. Neese, *Wiley Interdiscip. Rev.: Comput. Mol. Sci*. **2018**, *8*, e1327.

[70] F. Neese, F. Wennmohs, U. Becker, C. Riplinger, *J. Chem. Phys*. **2020**, *152*, 224108.

[71] A. Becke, *Phys. Rev. A* **1988**, *38*, 3098-3100.

[72] J. Perdew, *Phys. Rev. B Condens. Matter* **1986**, *33*, 8822-8824.

[73] F. Weigend, R. Ahlrichs, *Phys. Chem. Chem. Phys*. **2005**, *7*, 3297-3299.

[74] F. Weigend, *Phys. Chem. Chem. Phys*. **2006**, *8*, 1057-1065.

[75] V. Barone, M. Cossi, *J. Phys. Chem. A* **1998**, *102*, 1995-2001.

[76] A. Barrozo, M. Orio, *ChemSusChem*. **2019**, *12*, 4905-4915.

[77] A. D. Becke, *J. Chem. Phys*. **1993**, *98*, 5648-5652.

[78] C. Lee, W. Yang, R. G. Parr, *Phys. Rev. B* **1988**, *37*, 785-789.
[79] J. P. Perdew, Y. Wang, *Phys. Rev. B* **1992**, *45*, 13244-13249.
[80] M. Drosou, C. A. Mitsopoulou, M. Orio, D. A. Pantazis, *Magnetochemistry* **2022**, *8*, 36.
[81] R. J. Gómez-Piñeiro, D. A. Pantazis, M. Orio, *ChemPhysChem* **2020**, *21*, 2667-2679.
[82] M. E. Casida, in *Recent advances in density functional methods, Vol 1*. (Ed.: D. P Chong), World Scientific, Singapore, **2011**, pp. 155-192.
[83] R. E. Stratmann, G. E. Scuseria, M. J. Frisch, *J. Chem. Phys*. **1998**, *109*, 8218-8224.
[84] R. Bauernschmitt, R. Ahlrichs, *Chem. Phys. Lett*. **1996**, *256*, 454-464.
[85] S. Hirata, M. Head-Gordon, M. *Chem. Phys. Lett*. **1999**, *302*, 375-382.
[86] S. Hirata, M. Head-Gordon, *Chem. Phys. Lett*. **1999**, *314*, 291-299.
[87] F. Neese, *J. Chem. Phys*. **2001**, *115*, 11080-11096.

Entry for the Table of Contents

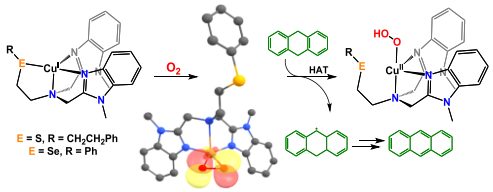

Copper complexes supported by thio- and selenoether ligands provide a coordination environment similar to the active sites of methionine-containing copper monooxygenases. Spectroscopic data, supported by theoretical studies, suggest that the chalcogenoethers act as hemilabile ligands, providing access to electrophilic side-on cupric superoxo intermediates capable of H-abstraction from dihydroanthracene. These results point at potential hemilability in methionine and selenomethionine-containing metalloenzymes.

Institute and/or researcher Twitter usernames: @Bioinorgani